



Nanoscale

Effect of liquid environment on single-pulse generation of laser induced periodic surface structures and nanoparticles

Journal:	<i>Nanoscale</i>
Manuscript ID	NR-ART-01-2020-000269.R1
Article Type:	Paper
Date Submitted by the Author:	29-Feb-2020
Complete List of Authors:	Shih, Cheng-Yu; University of Virginia, Department of Materials Science and Engineering Gnilitskyi, Iaroslav; Univ Modena , Shugaev, Maxim; University of Virginia, Material Science and Engineering Skoulas, Evangelos; Institute of Electronic Structure and Laser (IESL), Foundation for Research and Technology (FORTH) Stratakis, Emmanuel; IESL FORTH GR, Zhigilei, Leonid; University of Virginia, Department of Materials Science and Engineering

SCHOLARONE™
Manuscripts

Effect of liquid environment on single-pulse generation of laser induced periodic surface structures and nanoparticles

Cheng-Yu Shih,^{1,2} Iaroslav Gnilitzkiy,^{3,4,5} Maxim V. Shugaev,¹ Evangelos Skoulas,⁶
Emmanuel Stratakis⁶ and Leonid V. Zhigilei^{1,*}

¹ Department of Materials Science and Engineering, University of Virginia, 395 McCormick Road, Charlottesville, Virginia 22904-4745, USA

² Longterm Concept International Pte Ltd, 111 North Bridge Road #18-01, Peninsula Plaza, Singapore, 179098

³ “NoviNano Lab” LLC, 79000, Lviv, Ukraine

⁴ Department of Photonics, Lviv Polytechnic National University, 79013, Lviv, Ukraine

⁵ DISMI, University of Modena and Reggio Emilia (UNIMORE), 41122, Reggio Emilia, Italy

⁶ Institute of Electronic Structure and Laser (IESL), Foundation for Research and Technology (FORTH), N. Plastira 100, Vassilika Vouton, 70013, Heraklion, Crete, Greece

Abstract

The effect of a liquid environment on the fundamental mechanisms of surface nanostructuring and generation of nanoparticles by single pulse laser ablation is investigated in a closely integrated computational and experimental study. A large-scale molecular dynamics simulation of spatially-modulated ablation of Cr in water reveals a complex picture of dynamic interaction between the ablation plume and water, which involves rapid deceleration of the ablation plume by water environment, formation and prompt disintegration of a hot metal layer at the interface between the ablation plume and water, lateral redistribution and redeposition of a major fraction of the ablation plume, and eventual formation of smooth frozen surface features. A good agreement between the shapes of the surface features predicted in the simulation and the ones generated in single pulse laser ablation experiments performed for Cr in water supports the

* Corresponding Author
E-mail: lz2n@virginia.edu

mechanistic insights revealed in the simulations. The results of this study suggest that the presence of liquid environment can eliminate the sharp features of surface morphology, reduce the amount of material removed from the target by more than an order of magnitude, and narrow down the nanoparticle size distribution as compared to laser ablation in vacuum. Moreover, the computational predictions of the effective incorporation of molecules constituting the liquid environment into the surface region of the irradiated target and the generation of high vacancy concentrations exceeding the equilibrium levels by more than an order of magnitude suggest a potential for hyperdoping of laser-generated surfaces by solutes present in the liquid environment.

Keywords: Pulsed Laser Ablation in Liquids; Laser-Induced Periodic Surface Structures (LIPSS); Molecular Dynamics Simulations; Generation of Nanoparticles; Hyperdoping; Surface Morphology; Crystal Defects.

Surface nanostructuring is an effective way to drastically alter the chemical, mechanical, and optical properties of conventional materials and to achieve desired functionality in applications. The deterministic top-down nanofabrication techniques, such as electron or ion beam lithography,^{1,2} scanning probe writing utilizing the optical near field effects,^{3,4} or generation of surface features by tightly-focused ultrashort laser pulses⁵⁻⁷ are all suitable methods for forming high-resolution surface nanostructures. A common shortcoming of these methods, however, is a limited scalability and low processing speed, which limits their utilization in industrial applications. A faster surface nanostructuring can be achieved through irradiation by spatially overlapping ultrashort laser pulses, which can yield disordered hierarchical nano/micro-structured surface structures.⁸⁻¹² Moreover, a certain degree of regularity on the laser-processed surfaces can be introduced by spatial modulation of the energy deposition introduced through interference between multiple laser beams^{7,13,14} or naturally occurring interference of the incident laser beam and surface scattered electromagnetic waves,^{15,16} leading to the formation of laser-induced periodic surface structures (LIPSS).^{9-12,16-23}

It has been demonstrated that surfaces subjected to laser nanostructuring can possess unique properties, such as superhydrophobicity and self-cleaning,^{11,17,18} enhanced tribological performance,^{19,20} altered cell adhesion, growth and proliferation,^{21,22} as well as strongly modified optical properties.^{8,17,23} The progress in optimization and tuning of surface structures for the needs of practical applications, however, usually involves extensive experimentation with irradiation parameters, such as laser wavelength, polarization, pulse duration, fluence, repetition rate, scanning speed, and spot diameter. Moreover, since the generation of surface morphology in laser processing relies, to a large degree, on spontaneous material response to the rapid laser energy deposition, the precise control over the surface structures is not always possible to achieve.

An additional flexibility in tuning the surface morphology can be achieved by performing laser processing in a liquid environment. Indeed, it has been demonstrated in a number of studies that the choice of liquid can be effectively used to control the microstructure and morphology of laser-treated surfaces,²⁴⁻²⁹ which in turn has a strong effect on the ablation rate and nanoparticle production.³⁰ The lack of understanding of the fundamental mechanisms responsible for laser-assisted surface nanostructuring in liquids, however, hinders the effective utilization of the opportunities provided by this promising surface processing approach. The theoretical and

computational treatments of laser – material interactions in liquids have been largely focused on the generation of nanoparticles³¹⁻³⁶ and general mechanisms of laser ablation,^{34,37,38} with only a few studies addressing the effect of the liquid environment on generation of surface structures and subsurface defects.^{14,34,39} In particular, recent molecular dynamics (MD) simulations of laser interaction with Ag target in water have revealed the ability of the liquid environment to suppress the nucleation of subsurface voids and facilitate formation of a nanocrystalline surface structure upon melting and resolidification.³⁹ At higher fluences, the water environment has been shown to help to stabilize large subsurface voids leading to surface swelling,³⁴ whereas a thin liquid overlayer has been shown to partially suppress localized spallation from a Au target.¹⁴

In this article, we address the general question on the fundamental mechanisms responsible for laser-assisted surface nanostructuring in liquids by performing a closely integrated computational and experimental study of the generation of LIPSS in the ablative regime. The recent demonstration of the formation of highly regular LIPSS by a nearly single pulse irradiation at a laser fluence significantly above the ablation threshold^{40,41} not only suggests a viable surface processing technique capable of competing with current industrial surface processing methods,^{42,43} but also provides an opportunity to directly probe the effect of the liquid environment on the laser-generated surface morphology under well-controlled single pulse irradiation conditions. The process of spatially-modulated ablation of a Cr target in water is studied here in a large-scale MD simulation and in experiments performed for similar irradiation conditions. The simulation reveals a complex picture of dynamic interaction between the ablation plume and water, which has a dramatic effect on the lateral redistribution of the material and drastically alters the final shape of the surface structures in comparison with earlier results obtained in vacuum.⁴⁴ The shapes of the surface structures observed in experimental study of the single pulse LIPSS formation on a Cr surface irradiated in air and in water environment are in a good agreement with predictions of the atomistic modeling, thus supporting the mechanistic insights obtained in the simulations.

RESULTS AND DISCUSSION

The simulation and experiments reported in this paper are performed for a bulk single crystal Cr target with (100) surface orientation irradiated by a single 200 fs laser pulse. The incident fluence of 6000 J/m² used in experiments performed in air is well above the ablation threshold and corresponds to irradiation conditions where the formation of highly regular LIPSS

is observed in surface processing by weakly overlapping laser pulses.^{40,41} As can be seen from Figure 1a-c, which shows surface morphology produced in the central part of the laser spot, even a single pulse laser irradiation in this regime is capable of causing significant material redistribution and formation of surface patterns that serve as precursors for the formation of well-developed LIPSS upon surface scanning by overlapping laser pulses. The SEM image in Figure 1a reveals a sequence of parallel lines with noticeable periodicity, while an enlarged view of one of the lines provided in Figure 1b and a TEM image of a thin slice (lamella) extracted by FIB milling from a small region that cuts through one of these lines, shown in Figures 1b and 1c, respectively, expose a relatively sharp shape of the surface protrusion, with its height significantly exceeding its width. Since the spot illustrated by Figure 1a-c is irradiated by a single laser pulse, the produced quasi-periodic surface morphology is not defined by any preexisting periodic motif and clearly demonstrates the generation of LIPSS-like structures in a single pulse irradiation regime.

The incident laser fluence of 6000 J/m^2 can be converted to the absorbed fluence of 2200 J/m^2 by assuming a constant value of reflectivity of 0.63 for the wavelength of 1026 nm ⁴⁵ used in the experiment. This assumption can be justified by the relatively small (less than 10%) variation of the reflectivity in a range of electron temperature from zero to $25,000 \text{ K}$ predicted in *ab initio* simulations for the laser wavelength of 1030 nm .⁴⁶ A recent large-scale atomistic simulation of spatially-modulated ablation in vacuum⁴⁴ performed in a similar irradiation regime (20% modulation around an average level of 2500 J/m^2) has revealed a complex dynamic picture of material removal and redistribution leading to the formation of prominent surface features extending above the level of original surface of the irradiated target. Lateral pressure gradients in the plume generated by the spatially modulated laser ablation drive the vapor and liquid droplets to the regions located above the minima of the laser energy deposition at the target surface. The material redistribution leads to formation of a transient elongated liquid wall extending up to $\sim 600 \text{ nm}$ above the surface of the target. The upper part of the liquid wall disintegrates into droplets, while the base of the wall evolves into a relatively sharp protrusion captured by solidification on the time scale of $\sim 2 \text{ ns}$. The final height, thickness, and shape of the surface protrusion predicted in the simulation and shown in Figure 1d, are strikingly similar to those of the surface feature observed in the TEM image in Figure 1c. Moreover, a frozen liquid droplet at the top of the simulated surface protrusion is also present in the TEM image in Figure 1c, thus

supporting the mechanism of the ablative generation of LIPSS through disintegration of a transient liquid wall suggested by the simulation. Note that earlier simulations performed in 1 atm Ar atmosphere^{47,48} demonstrate that, while the presence of atmospheric background gas pressure affects the evolution of ablation plume and nanoparticle generation, it has no influence on the flow of molten material in the vicinity of the target surface and the final morphology of solidified target. This observation justifies the direct comparison of surface morphology predicted in the simulation performed in vacuum (Figure 1d) with experimental results obtained in air (Figure 1c).

To investigate the effect of the liquid environment on the laser-assisted surface nanostructuring, we performed a large-scale MD simulation of the single-pulse LIPSS formation in water under irradiation conditions similar to those used in vacuum (see Methods for the model description). The presence of the liquid environment above the Cr target drastically changes the dynamics of ablation plume expansion, as can be seen from atomistic snapshots shown in Figure 2 and the fields of density, concentration of water, and temperature depicted in Figure 3. Instead of the free expansion and lateral redistribution of the ablation plume observed in vacuum,⁴⁴ the hot mixture of vapor and liquid droplets produced in the explosive decomposition of the superheated Cr target is rapidly decelerated by the water environment and remains confined within just ~150 nm region above the irradiated surface. The top part of the ablation plume gets into direct contact with water and produces a narrow region where water superheated above its critical temperature is mixed with the Cr vapor. This narrow mixing region shows up at 100 ps as a thin green stripe in a plot of water concentration in Figure 3. The Cr atoms in this region are rapidly quenched and condense forming a nanogranular layer composed of atomic clusters and nanoparticles, which is apparent from the atomistic snapshots and density plots shown for 100 and 200 ps in Figures 2 and 3.

The initial upward motion of the ablation plume rapidly slows down and turns back within just 200 ps after the laser irradiation, as can be seen from the local momentum density (defined as a product of local velocity and mass density) vectors plotted on the density fields in Figure 3. At 200 ps, the relatively dense layer of Cr formed at the interface with water is still moving upwards, while the lower part of the plume is already reflected from the interface and moves down. Meanwhile, the pressure created by superheated water in the mixing region pushes the interfacial region down and, by the time of 500 ps, the Cr nanoparticles formed by

decomposition of the interfacial layer are already entrained into the hot supercritical water expanding towards the target surface.

The processes of plume reflection and redeposition proceed simultaneously with lateral material redistribution driven by strong pressure gradients generated in the course of spatially modulated ablation and directed towards the central part of the computational system, *i.e.*, the region located above the part of the target surface that received the minimum laser energy deposition. The pressure gradients drive the collective motion of Cr vapor and liquid droplets towards the center, as can be seen from the momentum density vectors in the ablation plume. The vectors have components directed towards the center both at the stage of the initial plume expansion and upon its reflection from the water environment, as can be seen from the density plots shown in Figure 3 for 100 and 200 ps, respectively. While at 100 ps the densest part of the ablation plume appears to be weakly connected to the target by a porous/foamy region, the lateral pressure gradients and material redistribution quickly compact this region, leading to the formation of a thick “wall” with continuous density distribution. In contrast to the spatially modulated ablation in vacuum, where the lateral material redistribution leads to the formation of an elongated thin liquid wall rapidly expanding in the vertical direction,⁴⁴ the presence of water environment suppresses the upward expansion of the plume and results in splashing of the top part of the wall into a wing-like transient structure seen at 500 ps in Figures 2 and 3.

The subsequent evolution of the shape of the liquid wall is strongly affected by the complete disintegration of the transient layer generated at the initial stage of the ablation process through accumulation of the ablation plume at the interface with water. The disintegration of the layer into individual nanoparticles occurs by ~500 ps and lets the supercritical water to stream towards the surface of the target, as can be seen from plots of water concentration shown in Figure 3 for 500 and 900 ps, and in Supporting Information for 700 ps. The water entrains the Cr nanoparticles, pushes the “wings” of the liquid wall/bump down, and contributes to smoothing the overall shape of the bump.

The mixing of water with hot ablation plume (Cr vapor and small clusters) confined near the surface of the target by the water environment results in a fast quenching of the plume and massive nucleation and growth of Cr nanoparticles. This process is reflected in the decrease in density of vapor-phase Cr atoms (red dots in Figure 2) as time progresses from 500 to 700 to 900

and to 1800 ps in Figure 2, as well as in the rapid cooling seen in the sequence of temperature profiles shown in Figure 3. While some of the nanoparticles are redeposited to the target, many are entrained into vortices that develop in the vapor cavity as the supercritical water flows along the semi-spherical bump of molten Cr, collides with the peripheral area, and causes an upward motion of vapor and nanoparticles, as can be seen from the momentum density arrows in the density plots shown in Figure 3 for 900 and 1500 ps, and in Supporting Information for 700 and 1200 ps. This motion leads to the expansion of the low-density hot region where the ablation plume is mixed with the supercritical water. This mixing region can be considered to be a precursor of the cavitation bubble typically observed in time-resolved experimental probing of pulsed laser ablation in liquids.⁴⁹⁻⁵¹

Many of the nanoparticles present in the mixing region at the initial stage of the cavitation bubble expansion studied in the simulation can be expected to end up in the water environment upon the bubble collapse, forming a colloidal solution above the irradiated surface of the target. The cluster analysis performed for an atomistic configuration produced by the end of the simulation at 2.2 ns, Figure 4, reveals a broad distribution of nanoparticle diameters ranging from 1 to 18 nm. While the nanoparticle size distribution shown in Figure 4 is likely to undergo further changes during the cavitation bubble expansion and collapse, it still provides an important insight into the origin of the final broad or even bimodal nanoparticle size distribution commonly observed in experimental studies of nanoparticle generation by laser ablation in liquids.^{35,52,53} Moreover, recent time-resolved X-ray probing of the cavitation bubbles⁵¹ indicates that large nanoparticles appear early in the ablation process and are present already at the advancing fronts of the expanding bubbles. These results suggest that the processes occurring at the initial stage of the ablation process are likely to play the key role in defining the final nanoparticle size distribution.

The majority of nanoparticles generated in the simulation are small, below 5 nm in diameter (Figure 4a), and are formed through rapid nucleation and growth in the region where Cr plume is quenched as a result of mixing with water. At the same time, most of the Cr material removed from the target is contained in much less numerous larger nanoparticles with diameter above 10 nm, as can be seen from Figure 4b, where the distribution is shown in terms of the number of atoms in nanoparticles of different sizes. As discussed above, these large nanoparticles originate from decomposition of the transient dense and hot Cr layer formed at the

interface with water environment. The generation of large nanoparticles in the course of decomposition of a dense layer generated at the metal-water interface has been observed in earlier MD simulations performed under conditions of spatially homogeneous laser energy deposition for thin Ag films³³ and bulk targets,^{34,35,36} where the layer roughening and disintegration was found to be facilitated by the Rayleigh-Taylor instability of the interface between the higher density metal layer decelerated by the pressure from the lighter supercritical water. In the case of the spatial modulation of laser energy deposition investigated in the present work, the lateral pressure gradients and the corresponding material redistribution in the ablation plume serve as a major additional factor leading to the rapid disintegration of the interfacial layer into nanoparticles. The prompt layer disintegration also prevents the formation of the largest nanoparticles that emerge from the much slower evolution and fragmentation of the flat dense layer occurring in the absence of the lateral disturbances. The computational prediction of the elimination of largest nanoparticles in spatially-modulated ablation suggests a possible approach for minimization of the material waste in the nanoparticle generation by laser ablation in liquids, which is of particular importance for precious metals.

By turning our attention from nanoparticle generation to the evolution of the surface morphology, we observe gradual smoothing of the shape of a surface bump generated by the lateral material redistribution and redeposition at the initial stage of the ablation process (*cf.* images for times after 700 ps in Figures 2 and 3). The smoothing of the bump is largely driven by surface tension and proceeds simultaneously with cooling and epitaxial regrowth of the crystalline target. The location of the advancing solidification front is marked by white dashed curves for times of 1.5 and 1.8 ns in Figures 3e and 2, respectively. The rapid advancement of the solidification front results in complete solidification of the bump by ~ 2.2 ns. The final shape of the frozen surface features a smooth hemicylindrical bump that rises ~ 65 nm above the lowest levels of the new surface in the valleys adjacent to the bump. This shape is very different from the one predicted in the simulation performed for the same irradiation conditions in vacuum, where the formation of an elongated protrusion with height exceeding 100 nm is observed, Figure 1d.

In addition to the distinct shapes of the surface protrusions formed in the single pulse spatially modulated laser ablation in water and vacuum, the effect of the environment strongly affects the total amount of material removed from the target. The ablation yield in the simulation

performed in vacuum is 22,868,721 atoms, which corresponds to the 24.6-nm-deep surface layer in the initial crystalline Cr target. The total amount of Cr that ends up mixed with supercritical water in the slowly expanding cavitation bubble is more than an order of magnitude lower, 1,764,198 Cr atoms, which corresponds to an equivalent 1.9-nm-thick layer of the initial target. The drastic drop of the ablation yield in the presence of water environment can be explained by the reflection of a major fraction of the ablation plume from the water-plume interface and redeposition of the material to the target. One implication of this observation is that surface processing in a liquid environment is a much more sparing in terms of the material waste, and may be preferable in applications where surface recession should be avoided and/or the ejection of ablation products present a health hazard.

In order to verify the computational predictions on the strong effect of liquid environment on the morphology of laser-processed surface, the experimental study of the ablative surface modification in air, discussed above and illustrated by Figure 1a-c, is extended to laser processing in water. Except for the environment, all other experimental conditions are kept the same, *i.e.*, single pulse irradiation of a single crystal Cr (100) surface at a wavelength of 1026 nm and an incident fluence of 6000 J/m². Surface morphology is characterized by SEM imaging and TEM analysis of a cross-sectional slice extracted from the laser spot, Figure 5. As can be seen from the SEM image of a surface region located near the center of the laser spot, Figure 5a, one of the most notable effect of the presence of water environment is the pronounced smoothing of the surface morphology, as compared to the one generated by ablation in air, Figure 1a. This observation agrees well with the results of the atomistic simulation that predict the formation of much smoother surface features in water as compare to vacuum conditions (*cf.* Figures 1d and 6).

The typical size of the surface features produced in the experiment conducted in water is approximately 500 nm, which is consistent with prior studies of LIPSS formation in water environment showing much shorter period of surface structures than the laser wavelength, in contrast to the LIPSS formation in vacuum.^{54,55} The typical elevation of the smooth bumps is ~100 nm, as illustrated by the TEM image of a cross-section cutting through several surface features shown in Figure 5b. Some of these features are remarkably similar to the ones predicted in the simulation, *cf.* Figures 5d and the last image in Figure 2. Other features, such as the one shown in Figure 5c, have shapes resembling frozen nano-wave. These unusual shapes can be attributed to uneven distribution of the laser energy deposition within the laser spot. In addition

to the periodic absorption pattern created by the interference of the incident and surface scattered electromagnetic waves,^{15,16} the Gaussian shape of the laser energy deposition profile leads to the emergence of global pressure gradients in the ablation plume confined by water. This pressure gradient is directed from center to the periphery of the laser spot and is likely to be responsible for splashing the surface features in this direction, as can be seen in Figures 5b and 5c.

The observation that frozen surface features generated in the simulation (Figure 2) and experiment (Figure 5d) not only have similar shapes but similar dimensions (height and width) as well is surprising, as the length-scale of the modulation of the laser energy deposition is substantially larger in experiment as compared to the simulation. This striking quantitative match of the dimensions of the laser-generated surface features suggests that, while the periodicity of ablative LIPSS is largely controlled by the laser wavelength, the shape and dimensions of the surface features are less sensitive to the laser wavelength and are defined by the ablation depth and the dynamics of the interaction of the ablation plume with water environment.

The good agreement between modeling and experiments on the effect of the water environment on surface morphology produced by single pulse laser ablation lends strong support to the notion that the mechanisms revealed in the simulations reflect the reality. It also encourages further analysis of laser-generated surface feature aimed at exposing the details of nanostructure that is difficult to probe experimentally. One finding from the analysis of the microstructure of the resolidified surface bump is that a substantial number of molecules constituting the liquid environment is incorporated into the bump, as can be seen from water density contour plot shown in Figure 7. The water is mainly present near the base of the bump, where clusters of nanobubbles filled with water are generated at the early stage of the bump formation, when the ablation plume is reflected from the water environment and redeposited to the target. The nanoscale water bubbles can also be clearly seen in Figure 6c, where both external and internal surfaces are shown by gray color, as well as in the density contour plots, *e.g.*, in a region outlined by the solid oval in Figure 3e. The water is also present throughout the surface region of the target, where it is more evenly distributed with the average water concentration in a 10-nm-thick surface layer of 0.017 wt.%. The effective incorporation of molecules constituting the liquid environment into the surface region of the irradiated target suggests a potential for hyperdoping (*i.e.*, doping far beyond the material solubility limit) of

laser-generated surface features by the liquid molecules or solutes present in the liquid environment. Indeed, the doping of oxide nanoparticles⁵⁶ and Si surface structures^{57,58} generated by laser ablation in liquids by elements added to liquid environment has recently been demonstrated experimentally.

The penetration of the solute deeper into the target may be facilitated by the vortexes transiently appearing in the molten bump structure and illustrated by arrows in the density plot shown for 900 ps in Figure 3d, as well as by the long-term solid-state diffusion in the resolidified surface region. The latter can be enhanced by the strong vacancy supersaturation generated in the course of laser-induced melting and resolidification. The distribution of vacancies and divacancies is shown in Figure 6a, while the larger vacancy clusters can be seen in Figure 6b, where the atoms with low potential energies are blanked, so that the dislocations and vacancy clusters are exposed. The average concentration of vacancies and divacancies within the surface bump is 0.218% and 0.0113%, respectively. This level of vacancy concentration is significantly above the equilibrium vacancy concentration at melting temperature ($\sim 0.01\%$), but is similar to the vacancy concentration observed in earlier atomistic simulations of laser processing of Cr targets in vacuum.^{44,59} The generation of strong vacancy supersaturation is attributed to the rapid propagation of the solidification front proceeding under conditions of strong undercooling below the equilibrium melting temperature, which has been shown to produce high vacancy concentrations.⁶⁰ The rapid solidification process also results in the formation of a network of dislocations. The dislocation configurations can be identified in Figure 6b, where the chains of atoms with elevated potential energy correspond to dislocation cores, as well as in Figure 6c, where the dislocation lines are identified with the dislocation extraction algorithm described in Ref. [61]. Similarly to the surface features generated by spatially modulated ablation in vacuum,⁴⁴ the dislocation network consists of dislocations with Burgers vector of $a/2 \langle 111 \rangle$ connected by several segments of $a \langle 100 \rangle$ dislocations, where a is the bcc lattice constant of Cr. The average dislocation density within the surface bump is $\sim 10^{15} \text{ m}^{-2}$.

SUMMARY

The fundamental mechanisms responsible for femtosecond laser induced surface nanostructuring and generation of nanoparticles by laser ablation in a liquid environment are investigated in a joint computational and experimental study performed for a bulk single crystal

Cr target irradiated by a single laser pulse in the regime of ablative LIPSS formation. A large-scale MD simulation of spatially-modulated ablation of Cr in water reveals a complex picture of dynamic interaction of the ablation plume with water, which has a dramatic effect on the lateral redistribution of the material and the final shape of the surface structures. Similar to the irradiation in vacuum, laser excitation and fast electron-phonon thermalization of the deposited energy leads to the rapid melting, superheating, and explosive decomposition of the top ~ 40 nm surface layer of Cr target into a mixture of vapor and liquid droplets (the process commonly referred to as phase explosion). Instead of the free expansion of the ablation plume observed in vacuum, however, the hot mixture of vapor and liquid droplets is rapidly decelerated by the water environment. Water in the contact with the ablation plume is heated well above its critical point, starts to expand, and pushes the hot metal layer accumulated at the interface between water and ablation plume back toward the target surface, leading to redeposition of the major part of the plume.

The processes of the plume reflection and redeposition proceed simultaneously with lateral material redistribution driven by pressure gradients generated in the course of spatially modulated ablation and directed towards the region at the minimum of the laser energy deposition. The lateral material redistribution and the vertical confinement of the plume by the water environment result in the formation of a thick wall-like structure that gradually evolves into a liquid bump with smooth shape and continuous density distribution. This evolution from the wall-like structure into a smooth bump is assisted by rupture and disintegration of the interfacial layer of hot molten metal generated at the water-plume interface, which allows the supercritical water to stream towards the surface of the target and to smooth-out the shape of the bump. The epitaxial regrowth of the crystalline part of the target results in complete solidification of ~ 65 -nm-tall bump by ~ 2.2 ns after the laser pulse. The final shape of the bump predicted in the simulation is remarkably similar to the one revealed in the TEM analysis of the surface morphology generated in the single pulse laser ablation experiments performed in water. The good agreement between modeling and experiments provides strong support for the mechanistic insights obtained in the simulation and described above. It also suggests that, in contrast to the periodicity of ablative LIPSS that scales with the laser wavelength, the shape and dimensions of the laser-generated surface features are less sensitive to the laser wavelength and

are largely defined by the ablation depth and the dynamics of the interaction of the ablation plume with water environment.

The results of the atomistic modeling reported in this paper not only provide insights into the complex dynamic processes involved in spatially-modulated laser ablation in liquids, but also reveal several general aspects of these processes that may have important practical implications. First and the most apparent conclusion of this study is that the presence of liquid environment tends to eliminate the sharp features of surface morphology produced in laser processing, thus suggesting the liquid environment as an effective experimental parameter to engineer the shape of LIPSS and other related nanostructures. Second, the total amount of material removed from the target and converted into colloidal nanoparticles is more than an order of magnitude lower in laser ablation in water as compared to the ablation yield predicted for similar irradiation conditions in vacuum. This observation suggests that surface nanostructuring in liquids may be preferable in applications where surface recession should be avoided and/or the ejection of ablation products present a health hazard. Third, the effective incorporation of molecules constituting the liquid environment into the surface region of the irradiated target, as well as the generation of strong vacancy supersaturation in the bump structure, predicted in the simulation, suggests a potential for hyperdoping of laser-generated surface features by solutes present in the liquid environment. Finally, the computational prediction of the prompt disintegration of the interfacial layer into nanoparticles assisted by the lateral pressure gradients suggests the spatially modulated ablation as an effective method for elimination of largest nanoparticles and minimization of the material waste in the nanoparticle generation by laser ablation in liquids.

METHODS

Computational Model. The simulation reported in this paper is performed for a bulk Cr target covered by water and irradiated by a femtosecond laser pulse with a spatially modulated laser energy deposition. A hybrid computational model^{62,63} combining a continuum level description of laser excitation of electrons followed by electron-phonon equilibration based on two temperature model⁶⁴ (TTM), a classical atomistic MD representation of the response of the Cr target to the fast energy deposition, and a coarse-grained (CG) MD representation of liquid environment parametrized for water is used in the simulation. The CG MD model combines the breathing sphere model developed for simulations of laser interaction with molecular systems⁶⁵

with a heat bath approach that associates an internal energy variable with each coarse-grained particle.^{33,34,66,67}

A schematic representation of the computational system is shown in Figure 8. The initial dimensions of the TTM-MD domain representing the Cr target are $260 \text{ nm} \times 43 \text{ nm} \times 140 \text{ nm}$, which corresponds to 131 million Cr atoms. The Cr target has bcc crystal structure and (001) surface orientation. The periodic boundary conditions are applied in the lateral directions, parallel to the surface of the target. The interatomic interactions are described by the embedded atom method (EAM) potential parametrized for Cr.⁵⁹ The electronic heat transfer in the deeper part of the target, where no structural changes are expected, is described based on the conventional TTM approach. The depth covered by the TTM is chosen to be $2.5 \mu\text{m}$ to ensure a negligible temperature change at the bottom of the computational system by the end of the simulation.

Above the bulk Cr target, the water environment is represented by a 300-nm-thick layer of CG MD (37.4 million CG particles) covered by dynamic acoustic impedance matching boundary condition based on an imaginary plane approach described in Ref. [68] (denoted as nonreflecting boundary, NRB in Figure 8). The cross-interaction between Cr and CG water is described with LJ potential with energy parameter ϵ fitted to the experimental values of Cr-water interfacial energy^{69,70} and length parameter σ taken as average of the equilibrium distances between CG water particles and EAM Cr. At the bottom of the TTM-MD part of the model, a recently developed Langevin nonreflecting boundary (LNRB) condition⁴⁴ is applied. This boundary condition ensures nonreflective propagation of the laser-induced pressure waves even in the case of non-planar waves generated in spatially modulated laser ablation. The application of NRB and LNRB enables an adequate representation of experimental conditions in laser ablation of a bulk target covered by a thick liquid layer, where the reflections of the pressure waves from the back surface of the irradiated target and the outer surface of the water layer do not have any effect on the processes responsible for surface modification, using computationally tractable sizes of the TTM-MD and CG MD parts of the model.

The thermophysical properties of Cr entering the TTM equations are as follows. The electron heat capacity of Cr is approximated as $C_e = \gamma T_e$ with $\gamma = 194 \text{ Jm}^{-3}\text{K}^{-2}$.⁷¹ Constant values of the electron-phonon coupling factor, $G = 4.2 \times 10^{17} \text{ Wm}^{-3}\text{K}^{-1}$,⁷² and the lattice heat capacity,

$C_l = 3.23 \times 10^6 \text{ Jm}^{-3}\text{K}^{-1}$,⁷³ are assumed in the simulation. The temperature dependence of the electron thermal conductivity is approximated by the Drude model relationship, $K_e(T_e, T_l) = v^2 C_e(T_e) \tau_e(T_e, T_l) / 3$, where $C_e(T_e)$ is the electron heat capacity, v^2 is the mean square velocity of the electrons contributing to the electron heat conductivity, approximated as the Fermi velocity squared, v_F^2 , and $\tau_e(T_e, T_l)$ is the total electron scattering time defined by the electron-electron scattering rate, $1/\tau_{e-e} = AT_e^2$, and the electron-phonon scattering rate, $1/\tau_{e-ph} = BT_l$, so that $1/\tau_e = AT_e^2 + BT_l$. The value of the coefficient $A = 2.66 \times 10^6 \text{ K}^{-2}\text{s}^{-1}$ is estimated with the free electron model,⁷⁴ while the coefficient B is described as a function of the lattice temperature and the phase state of the material, so that the experimental temperature dependence of thermal conductivity of Cr under conditions of electron-phonon equilibrium⁷⁵ is reproduced for both solid and liquid states. In particular, this description accounts for the two-fold drop of thermal conductivity as the temperature increases from 300 K to the melting point.

The laser irradiation is represented through a source term added to the TTM equation for the electron temperature.⁶² The source term has a temporal Gaussian profile corresponding to 200 fs pulse and accounts for the exponential attenuation of the deposited laser energy with depth. The optical absorption depth of Cr is equal to 9.6 nm at the wavelength 258 nm.⁴⁵ The absorbed laser fluence is spatially modulated along the x -direction to represent the periodic absorption pattern generated by the interference of the incident laser wave and surface scattered electromagnetic waves responsible for the LIPSS formation.^{15,16} We note that, in a more controlled manner, the spatial modulation of the laser energy deposition can be achieved through interference between multiple laser beams focused on the same laser spot.^{7,13,14} The period of the sinusoidal modulation is 260 nm, which matches the size of the computational cell in x -direction. The maximum and minimum absorbed fluences are 2000 to 3000 J/m^2 , which corresponds to 20% modulation of the laser energy deposition with respect to the average level of 2500 J/m^2 . This average fluence is more than 60% above the phase explosion threshold of 1500 J/m^2 established in a series of small-scale simulations of 200 fs laser pulse irradiation of Cr in vacuum. Before applying the laser irradiation, the whole system shown in Figure 8 is thermalized at 300 K for 300 ps.

Experimental setup. The experiments are performed in a single pulse laser ablation irradiation regime for a single crystal Cr target with (001) surface orientation, *i.e.*, for conditions similar to those studied computationally. The laser irradiation was done with an Yb:KGW laser source emitting linearly polarized pulses with pulse duration of 200 fs, 1 kHz repetition rate, and 1026 nm central wavelength. The experimental setup shown in Figure 9 also includes a system of a half-waveplates (HW) and a linear polarizer (LP) used to adjust the laser power, a dichroic mirror (DM) to guide the beam, a plano-convex lens (CL) with focal distance of 200 mm to focus the beam onto the sample, and a CMOS camera to observe the sample surface. The sample was placed in a small cell filled with distilled water covering the surface of the sample and up to 0.5 mm above. Then, the cell was set on a computer controlled 3-axis translational stage. The spot size was measured and calculated to be $\sim 32 \mu\text{m}$ in diameter at $1/e^2$ using a CCD camera on the focal plane within the lens Rayleigh range. The incident laser fluence of individual laser pulses is estimated to be 6000 J/m^2 for irradiation in both air and water environments. In all experiments, the normal direction of laser incidence with S-polarization with respect to the sample surface was used. The morphology of the laser-induced structures was analyzed by JEOL JSM-7500F SEM and FEI 80-300 kV Titan TEM/STEM microscopes.

Acknowledgments: The authors gratefully acknowledge Dr. Helge Heinrich of University of Virginia for his help with SEM and TEM analysis. Financial support for this work was provided by the National Science Foundation (NSF) through Grants CMMI-1663429 and DMR-1610936. Computational support was provided by the Oak Ridge Leadership Computing Facility (INCITE project MAT130) and NSF through the Extreme Science and Engineering Discovery Environment (project TG-DMR110090). L.V.Z. also acknowledges the Mercator Fellowship at the University of Duisburg-Essen, Germany, and I.G. acknowledges the support of Nanoscience Foundries & Fine Analysis (NFFA.eu) for Individual Fellowship under grant agreement ID323.

Supporting Information

Supporting information is provided in the form of a set of Power Point slides and contains the following images and animations:

A. Animated sequences of snapshots from the simulation illustrated by Figure 2 in the paper;

- B. Contour plots of density, water concentration, and temperature shown for a time of 100 ps after the laser pulse;
- C. Contour plots of density, water concentration, and temperature shown for times of 200, 500, and 700 ps;
- D. Contour plots of density, water concentration, and temperature shown for times of 900, 1200, and 1500 ps;
- E. Nanoparticle size distributions predicted in simulations of spatially modulated ablation of Cr in water and vacuum;
- F. Images of surface features produced in experiments and simulations of single pulse laser ablation of Cr in water and air/vacuum.

References

1. I. Utke, S. Moshkalev, and P. Russell (editors), *Nanofabrication Using Focused Ion and Electron Beams: Principles and Applications* (Oxford University Press, New York, NY, 2012), 812 pages.
2. W. Yue, Z. Wang, Y. Yang, L. Chen, A. Syed, K. Wong, and X. Wang, Electron-beam lithography of gold nanostructures for surface-enhanced Raman scattering, *J. Micromech. Microeng.* **22**, 125007 (2012).
3. C. P. Grigoropoulos, D. J. Hwang, and A. Chimmalgi, Nanometer-scale laser direct-write using near-field optics, *MRS Bull.* **32**, 16-22 (2007).
4. S. M. Huang, M. H. Hong, B. Lukiyanchuk, and T. C. Chong, Nanostructures fabricated on metal surfaces assisted by laser with optical near-field effects, *Appl. Phys. A* **77**, 293-296 (2003).
5. A. I. Kuznetsov, J. Koch and B. N. Chichkov, Nanostructuring of thin gold films by femtosecond lasers, *Appl. Phys. A* **94**, 221-230 (2009).
6. A. Naghilou, M. He, J. S. Schubert, L. V. Zhigilei, and W. Kautek, Femtosecond laser generation of microbumps and nanojets on single and bilayer Cu/Ag thin films, *Phys. Chem. Chem. Phys.* **21**, 11846-11860 (2019).
7. Y. Nakata, N. Miyanaga, and T. Okada, Effect of pulse width and fluence of femtosecond laser on the size of nanobump array, *Appl. Surf. Sci.* **253**, 6555-6557 (2007).
8. J. V. Oboňa, V. Ocelík, J. C. Rao, J. Z. P. Skolski, G. R. B. E. Römer, A. J. Huis in 't Veld, and J. Th. M. De Hosson, Modification of Cu surface with picosecond laser pulses, *Appl. Surf. Sci.* **303**, 118-124 (2014).
9. A. Y. Vorobyev and C. Guo, Enhanced absorptance of gold following multipulse femtosecond laser ablation, *Phys. Rev. B* **72**, 195422 (2005).
10. A. Abou-Saleh, E. T. Karim, C. Maurice, S. Reynaud, F. Pigeon, F. Garrelie, L. V. Zhigilei, and J. P. Colombier, Spallation-induced roughness promoting high spatial frequency nanostructure formation on Cr, *Appl. Phys. A* **124**, 308 (2018).
11. V. Zorba, E. Stratakis, M. Barberoglou, E. Spanakis, P. Tzanetakis, S. H. Anastasiadis, and C. Fotakis, Biomimetic artificial surfaces quantitatively reproduce the water repellency of a lotus leaf, *Adv. Mater.* **20**, 4049-4054 (2008).
12. Q.-Z. Zhao, S. Malzer, and L.-J. Wang, Self-organized tungsten nanospikes grown on subwavelength ripples induced by femtosecond laser pulses, *Opt. Express* **15**, 15741-15746 (2007).
13. J. Bekesi, P. Simon, and J. Ihlemann, Deterministic sub-micron 2D grating structures on steel by UV-fs-laser interference patterning, *Appl. Phys. A* **114**, 69-73 (2014).
14. D. S. Ivanov, A. Blumenstein, J. Ihlemann, P. Simon, M. E. Garcia, and B. Rethfeld, Molecular dynamics modeling of periodic nanostructuring of metals with a short UV laser pulse under spatial confinement by a water layer, *Appl. Phys. A* **123**, 744 (2017).

15. J. E. Sipe, J. F. Young, J. S. Preston, and H. M. van Driel, Laser-induced periodic surface structure. I. Theory, *Phys. Rev. B* **27**, 1141-1154 (1983).
16. J. Bonse, A. Rosenfeld, and J. Krüger, On the role of surface plasmon polaritons in the formation of laser-induced periodic surface structures upon irradiation of silicon by femtosecond-laser pulses, *J. Appl. Phys.* **106**, 104910 (2009).
17. A. Y. Vorobyev and C. Guo, Multifunctional surfaces produced by femtosecond laser pulses, *J. Appl. Phys.* **117**, 033103 (2015).
18. T. Baldacchini, J. E. Carey, M. Zhou, and E. Mazur, Superhydrophobic surfaces prepared by microstructuring of silicon using a femtosecond laser, *Langmuir* **22**, 4917-4919 (2006).
19. J. Bonse, S. Kirner, M. Griepentrog, D. Spaltmann, and J. Krüger, Femtosecond laser texturing of surfaces for tribological applications, *Materials* **11**, 801 (2018)
20. J. Eichstädt, G. R. B. E. Römer, and A. J. H. in't Veld, Towards friction control using laser-induced periodic surface structures, *Phys. Procedia* **12**, 7-15 (2011).
21. Ch. Yiannakou, Ch. Simitzi, A. Manousaki, C. Fotakis, A. Ranella, and E. Stratakis, Cell patterning via laser micro/nano structured silicon surfaces, *Biofabrication* **9**, 025024 (2017).
22. I. Gnilitzkyi, M. Pogorielov, R. Viter, A. M. Ferraria, A. P. Carapeto, O. Oleshko, L. Orazi, O. Mishchenko, Cell and tissue response to nanotextured Ti6Al4V and Zr implants using high-speed femtosecond laser-induced periodic surface structures, *Nanomedicine: NBM* **21**, 102036 (2019).
23. A. Papadopoulos, E. Skoulas, A. Mimidis, G. Perrakis, G. Kenanakis, G. D. Tsihidis, and E. Stratakis, Biomimetic omnidirectional antireflective glass via direct ultrafast laser nanostructuring, *Adv. Mater.* **31**, 1901123 (2019).
24. E. Stratakis, V. Zorba, M. Barberoglou, C. Fotakis, and G. A. Shafeev, Laser writing of nanostructures on bulk Al via its ablation in liquids, *Nanotechnology* **20**, 105303 (2009).
25. E. V. Barmina, E. Stratakis, K. Fotakis, and G. Shafeev, Generation of nanostructures on metals by laser ablation in liquids: new results, *Quantum Electron.* **40**, 1012-1020 (2010).
26. G. K. Podagatlapalli, S. Hamad, S. Sreedhar, S. P. Tewari, and S. V. Rao, Fabrication and characterization of aluminum nanostructures and nanoparticles obtained using femtosecond ablation technique, *Chem. Phys. Lett.* **530**, 93-97 (2012).
27. S. Bashir, M. S. Rafique, C. S. Nathala, W. Husinsky, Surface and structural modifications of titanium induced by various pulse energies of a femtosecond laser in liquid and dry environment, *Appl. Phys. A* **114**, 243-251 (2014).
28. D. Zhang, B. Gökce, S. Sommer, R. Streubel, and S. Barcikowski, Debris-free rear-side picosecond laser ablation of thin germanium wafers in water with ethanol, *Appl. Surf. Sci.* **367**, 222-230 (2016).
29. N. Lasemi, U. Pacher, L. V. Zhigilei, O. Bomati-Miguel, R. Lahoz, and W. Kautek, Pulsed laser ablation and incubation of nickel, iron and tungsten in liquids and air, *Appl. Surf. Sci.* **433**, 772-779 (2018).

30. R. Nadarajah, S. Barcikowski, and B. Gökce, Picosecond laser-induced surface structures on alloys in liquids and their influence on nanoparticle productivity during laser ablation, *Opt. Express* **28**, 2909-2924 (2020).
31. T. E. Itina, On nanoparticle formation by laser ablation in liquids, *J. Phys. Chem. C* **115**, 5044-5048 (2011).
32. M. E. Povarnitsyn, T. E. Itina, P. R. Levashov, and K. V. Khishchenko, Mechanisms of nanoparticle formation by ultra-short laser ablation of metals in liquid environment, *Phys. Chem. Chem. Phys.* **15**, 3108-3114 (2013).
33. C.-Y. Shih, C. Wu, M. V. Shugaev, and L. V. Zhigilei, Atomistic modeling of nanoparticle generation in short pulse laser ablation of thin metal films in water, *J. Colloid Interface Sci.* **489**, 3-17 (2017).
34. C.-Y. Shih, M. V. Shugaev, C. Wu, and L. V. Zhigilei, Generation of subsurface voids, incubation effect, and formation of nanoparticles in short pulse laser interactions with bulk metal targets in liquid: Molecular dynamics study, *J. Phys. Chem. C* **121**, 16549-16567 (2017).
35. C.-Y. Shih, R. Streubel, J. Heberle, A. Letzel, M. V. Shugaev, C. Wu, M. Schmidt, B. Gökce, S. Barcikowski, and L. V. Zhigilei, Two mechanisms of nanoparticle generation in picosecond laser ablation in liquids: the origin of the bimodal size distribution, *Nanoscale* **10**, 6900-6910 (2018).
36. C.-Y. Shih, M. V. Shugaev, C. Wu, and L. V. Zhigilei, The effect of pulse duration on nanoparticle generation in pulsed laser ablation in liquids: Insights from large-scale atomistic simulations, *Phys. Chem. Chem. Phys.*, in press (2020).
37. M. E. Povarnitsyn and T. E. Itina, Hydrodynamic modeling of femtosecond laser ablation of metals in vacuum and in liquid, *Appl. Phys. A* **117**, 175-178 (2014).
38. Yu. V. Petrov, V. A. Khokhlov, V. V. Zhakhovsky, and N. A. Inogamov, Hydrodynamic phenomena induced by laser ablation of metal into liquid, *Appl. Surf. Sci.* **492**, 285-297 (2019).
39. M. V. Shugaev, C.-Y. Shih, E. T. Karim, C. Wu, and L. V. Zhigilei, Generation of nanocrystalline surface layer in short pulse laser processing of metal targets under conditions of spatial confinement by solid or liquid overlayer, *Appl. Surf. Sci.* **417**, 54-63 (2017).
40. I. Gnilitzkyi, V. Gruzdev, N. M. Bulgakova, T. Mocek and L. Orazi, Mechanisms of high-regularity periodic structuring of silicon surface by sub-MHz repetition rate ultrashort laser pulses, *Appl. Phys. Lett.* **109**, 143101 (2016).
41. I. Gnilitzkyi, T. J.-Y. Derrien, Y. Levy, N. M. Bulgakova, T. Mocek, and L. Orazi, High-speed manufacturing of highly regular femtosecond laser-induced periodic surface structures: physical origin of regularity, *Sci. Rep.* **7**, 8485 (2017).
42. X.-M. Li, D. Reinhoudt, and M. Crego-Calama, What do we need for a superhydrophobic surface? A review on the recent progress in the preparation of superhydrophobic surfaces, *Chem. Soc. Rev.* **36**, 1350-1368 (2007).

43. E. Jiaqiang, Y. Jin, Y. Deng, W. Zuo, X. Zhao, D. Han, Q. Peng, and Z. Zhang, Wetting models and working mechanisms of typical surfaces existing in nature and their application on superhydrophobic surfaces: A review, *Adv. Mater. Interfaces* **5**, 1701052 (2018).
44. M. V. Shugaev, I. Gnilitzkiy, N. M. Bulgakova, and L. V. Zhigilei, Mechanism of single-pulse ablative generation of laser-induced periodic surface structures, *Phys. Rev. B* **96**, 205429 (2017).
45. E. D. Palik (editor), *Handbook of Optical Constants of Solids* (Academic Press, 1998).
46. E. Bévilion, R. Stoian, and J. P. Colombier, Nonequilibrium optical properties of transition metals upon ultrafast electron heating, *J. Phys.: Condens. Matter* **30**, 385401 (2018).
47. H. Wu, C. Wu, N. Zhang, X. Zhu, X. Ma, and L. V. Zhigilei, Experimental and computational study of the effect of 1 atm background gas on nanoparticle generation in femtosecond laser ablation of metals, *Appl. Surf. Sci.* **435**, 1114-1119 (2018).
48. C.-Y. Shih, C. Wu, H. Wu, M. V. Shugaev, and L. V. Zhigilei, in *Pulsed Laser Ablation: Advances and Applications in Nanoparticles and Nanostructuring Thin Films*, edited by I. N. Mihailescu, and A. P. Caricato (Pan Stanford, Singapore, 2018), pp. 421-426.
49. S. Ibrahimkutty, P. Wagener, T. dos Santos Rolo, D. Karpov, A. Menzel, T. Baumbach, S. Barcikowski, and A. Plech, A hierarchical view on material formation during pulsed-laser synthesis of nanoparticles in liquid, *Sci. Rep.* **5**, 16313 (2015).
50. J. Lam, J. Lombard, C. Dujardin, G. Ledoux, S. Merabia, and D. Amans, Dynamical study of bubble expansion following laser ablation in liquids, *Appl. Phys. Lett.* **108**, 074104 (2016).
51. S. Reich, A. Letzel, A. Menzel, N. Kretzschmar, B. Gökce, S. Barcikowski, and A. Plech, Early appearance of crystalline nanoparticles in pulsed laser ablation in liquids dynamics, *Nanoscale* **11**, 6962-6969 (2019).
52. J.-P. Sylvestre, A. V. Kabashin, E. Sacher, and M. Meunier, Femtosecond laser ablation of gold in water: influence of the laser-produced plasma on the nanoparticle size distribution, *Appl. Phys. A* **80**, 753-758 (2005)
53. G. Marzun, J. Nakamura, X. Zhang, S. Barcikowski and P. Wagener, Size control and supporting of palladium nanoparticles made by laser ablation in saline solution as a facile route to heterogeneous catalysts, *Appl. Surf. Sci.* **348**, 75-84 (2015).
54. C. Albu, A. Dinescu, M. Filipescu, M. Ulmeanu, and M. Zamfirescu, Periodical structures induced by femtosecond laser on metals in air and liquid environments, *Appl. Surf. Sci.* **278**, 347-351 (2013).
55. E. Stratakis, Nanomaterials by ultrafast laser processing of surfaces, *Sci. Adv. Mater.* **4**, 407-431 (2012).
56. A. Chemin, J. Lam, G. Laurens, F. Trichard, V. Motto-Ros, G. Ledoux, V. Jarý, V. Laguta, M. Nikl, C. Dujardin, and D. Amans, Doping nanoparticles using pulsed laser ablation in a liquid containing the doping agent, *Nanoscale Adv.* **1**, 3963-3972 (2019).
57. A. A. Ionin, S. I. Kudryashov, S. V. Makarov, N. N. Mel'nik, A. A. Rudenko, P. N. Saltuganov, L. V. Seleznev, D. V. Sinitsyn, I. A. Timkin, and R. A. Khmel'nik, Structural

- and electrical characteristics of a hyperdoped silicon surface layer with deep donor sulfur states, *JETP Lett.* **100**, 55-58 (2014).
58. L. V. Nguyen, S. I. Kudryashov, A. A. Rudenko, R. A. Khmel'nitskii, and A. A. Ionin, Separation of mid-IR light trapping and sulfur-donor absorption in nanosecond-laser sulfur-hyperdoped silicon: a way to spatially- and spectrally-engineered interband IR-absorption, *J. Russ. Laser Res.* **39**, 192-199 (2018).
 59. Z. Lin, R. A. Johnson, and L. V. Zhigilei, Computational study of the generation of crystal defects in a bcc metal target irradiated by short laser pulses, *Phys. Rev. B* **77**, 214108 (2008).
 60. M. He, C. Wu, M. V. Shugaev, G. D. Samolyuk, and L. V. Zhigilei, Computational study of short-pulse laser-induced generation of crystal defects in Ni-based single-phase binary solid-solution alloys, *J. Phys. Chem. C* **123**, 2202-2215 (2019).
 61. A. Stukowski and K. Albe, Dislocation detection algorithm for atomistic simulations, *Modelling Simul. Mater. Sci. Eng.* **18**, 025016 (2010).
 62. D. S. Ivanov and L. V. Zhigilei, Combined atomistic-continuum modeling of short-pulse laser melting and disintegration of metal films, *Phys. Rev. B* **68**, 064114 (2003).
 63. C. Wu and L. V. Zhigilei, Microscopic mechanisms of laser spallation and ablation of metal targets from large-scale molecular dynamics simulations, *Appl. Phys. A* **114**, 11-32 (2014).
 64. S. I. Anisimov, B. L. Kapeliovich, and T. L. Perel'man, Electron emission from metal surfaces exposed to ultrashort laser pulses, *Sov. Phys. JETP* **39**, 375-377 (1974).
 65. L. V. Zhigilei, E. Leveugle, B. J. Garrison, Y. G. Yingling, and M. I. Zeifman, Computer simulations of laser ablation of molecular substrates, *Chem. Rev.* **103**, 321-347 (2003).
 66. M. Tabetah, A. Matei, C. Constantinescu, N. P. Mortensen, M. Dinescu, J. Schou, and L. V. Zhigilei, The minimum amount of "matrix" needed for matrix-assisted pulsed laser deposition of biomolecules, *J. Phys. Chem. B* **118**, 13290-13299, 2014.
 67. J. Zou, C. Wu, W. D. Robertson, L. V. Zhigilei, and R. J. D. Miller, Molecular dynamics investigation of desorption and ion separation following picosecond infrared laser (PIRL) ablation of an ionic aqueous protein solution, *J. Chem. Phys.* **145**, 204202, 2016.
 68. E. T. Karim, M. Shugaev, C. Wu, Z. Lin, R. F. Hainsey, and L. V. Zhigilei, Atomistic simulation study of short pulse laser interactions with a metal target under conditions of spatial confinement by a transparent overlayer, *J. Appl. Phys.* **115**, 183501 (2014).
 69. J. Drelich, E. Chibowski, D. D. Meng, and K. Terpilowski, Hydrophilic and superhydrophilic surfaces and materials, *Soft Matter* **7**, 9804-9828 (2011).
 70. J. N. Israelachvili, *Intermolecular and Surface Forces*, 2nd edition (Academic Press, London, 1991).
 71. C. Kittel, *Introduction to Solid State Physics*, 7th edition (Wiley, New York, 1996).
 72. S. D. Brorson, A. Kazeroonian, J. S. Moodera, D. W. Face, T. K. Cheng, E. P. Ippen, M. S. Dresselhaus, and G. Dresselhaus, Femtosecond room-temperature measurement of the electron-phonon coupling constant γ in metallic superconductors, *Phys. Rev. Lett.* **64**, 2172-2175 (1990).

73. W. M. Haynes, *Handbook of Chemistry and Physics*, 97th edition (CRC Press, Boca Raton, Florence, 2016).
74. R. H. M. Groeneveld, R. Sprik, and A. Lagendijk, Femtosecond spectroscopy of electron-electron and electron-phonon energy relaxation in Ag and Au, *Phys. Rev. B* **51**, 11433-11445 (1995).
75. K. C. Mills, B. J. Monaghan, and B. J. Keene, Thermal conductivities of molten metals: Part 1 Pure metals, *Int. Mater. Rev.* **41**, 209-242 (1996).

Figure Captions

Figure 1. Surface morphology generated on a Cr (001) target irradiated *in air* by a single 200 fs laser pulse at an incident laser fluence of 6000 J/m^2 and illustrated here by two SEM images of the surface (a,b) and a TEM image of a cross-sectional slice extracted from a surface area that includes a protrusion generated by the laser irradiation (c). The shape of the surface protrusion in (c) can be related to the shape of a frozen surface feature and obtained in a large-scale MD simulation of spatially-modulated laser ablation of Cr (001) target performed in vacuum under irradiation conditions similar to those used in the experiment (d).

Figure 2. Snapshots of atomic configurations predicted in a simulation of a bulk Cr target irradiated *in water* by a 200 fs laser pulse at an averaged absorbed fluence of 2500 J/m^2 with 20% of energy modulation. Only parts of the computational system from 60 nm below the initial surface of the Cr target up to 240 nm above the surface are shown in the snapshots. The atoms are colored according to their potential energies, from blue for molten Cr to red for vapor-phase Cr atoms. The molecules representing water environment are blanked and the presence of water is illustrated schematically by a light blue region above the Cr target. White dashed lines in the snapshots shown for 1800 ps mark the location of solidification front. An animated sequence of snapshots from this simulation can be found in the Supporting Information.

Figure 3. Contour plots of density, water concentration, and temperature shown for different times in the simulation of spatially modulated ablation of Cr in water illustrated in Figure 2. The arrows in the density plots indicate the direction and the relative magnitude of the local momentum density. The length of the vectors is scaled up with respect to ones shown for 100 ps by a factor of 1.67 in plots shown for 200 and 500 ps and by a factor of 13.3 in plots shown for 900 and 1500 ps. Only parts of the computational system from -43 nm to 193 nm with respect to the initial surface of the Cr target are shown. Black ellipse in the density plot shown for 1500 ps outlines a region with several water nanobubbles captured during plume redeposition. White dashed lines in the same plot show the location of solidification front. Additional contour plots for times 700 and 1200 ps are provided in Supporting Information.

Figure 4. Nanoparticle size distribution predicted in the simulation of spatially modulated ablation of Cr in water illustrated in Figure 2. The distributions are shown for a time of 2.2 ns after the laser pulse. The number of nanoparticles of different sizes and the total number of atoms in the nanoparticles of the corresponding sizes are shown in (a) and (b), respectively. Atomic clusters with equivalent diameters smaller than 1 nm are not included in the distributions.

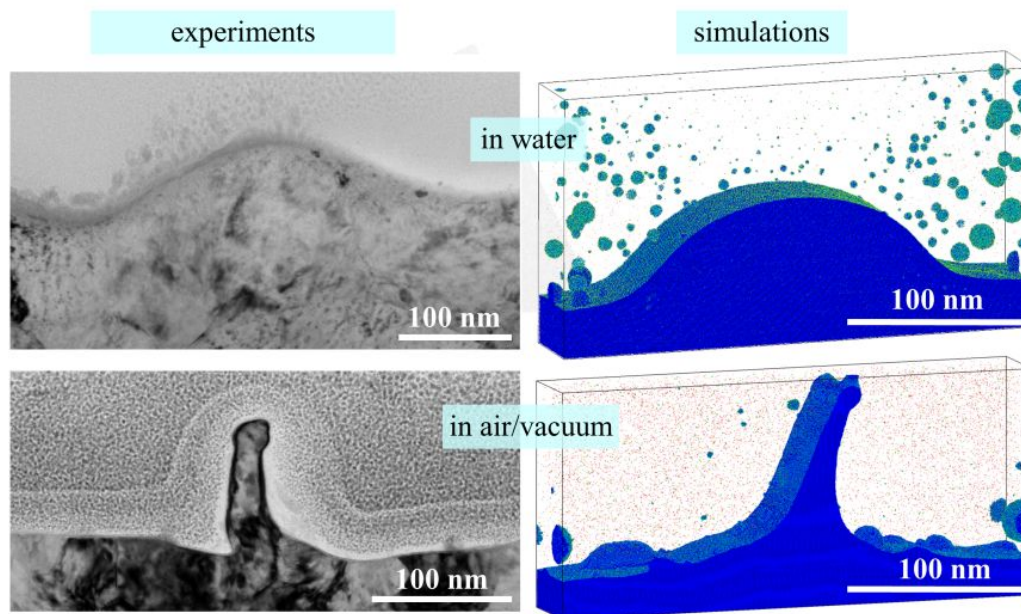
Figure 5. Surface morphology generated on a Cr (001) target irradiated *in water* by a single 200 fs laser pulse at an incident laser fluence of 6000 J/m² and illustrated here by an SEM image of the surface (a) and a TEM image of a cross-sectional slice extracted from the laser spot (b). Enlarged images of two regions outlined by dashed rectangles in (b) are shown in (c) and (d).

Figure 6. Three representations of the microstructure of the surface region of the irradiated Cr target at 2200 ps, after complete resolidification of the target. In (a), the atoms surrounding vacancies and divacancies are shown by blue and red color, respectively. In (b), dislocations and vacancy clusters present in and below the frozen bump are exposed by blanking the atoms with the potential energy below -3.94 eV (correspond to atoms with bcc local coordination and atoms surrounding single vacancies), and the remaining atoms are colored by their potential energy with color scale ranging from -4.0 eV (blue) to -3.4 eV (red). In (c), dislocations identified with the algorithm described in Ref. [61] are shown and colored by dislocation type. Gray color in this panel outlines the free surface of the Cr target, clusters of vacancies (gray dots), and surfaces of voids (gray spheres) formed as a result of entrapment of water vapor during plume redeposition. The box outlines the shape of the original target before the laser irradiation. Before the structural analysis, the system is quenched for 1 ps using the velocity dampening technique.

Figure 7. Contour plot of water concentration in the surface bump generated in the simulation illustrated in Figures 2, 3, and 6 by the time of 1500 ps, when the bump is still in the molten state. The contour plot is shown on the logarithmical scale that reveals the incorporation of water into the surface layer of the bump. The water molecules and nanobubbles at the base of the bump are trapped by the rapid solidification process, suggesting that laser processing in liquids can be used as a way to achieve hyperdoping of surface region of the irradiated target by molecules present in the liquid environment.

Figure 8. Schematic representation of the computational setup used in the simulation of single pulse ablative LIPSS formation with water environment. An atomistic snapshot from the simulation at 500 ps after the laser irradiation is used as background in the representation of the atomistic (TTM-MD) part of the model. Only parts of the computational system from -60 nm with respect to the initial surface of the Cr target are shown in the snapshot. The atoms are colored according to their potential energies, from blue for molten Cr to red for vapor-phase Cr atoms. The molecules representing water environment are blanked, and the presence of water is illustrated schematically by a light blue region labeled as CG-water. The black curve shows schematically the modulation of the laser energy deposition along the x -direction. The continuum part of the model, and dimensions of the atomistic and continuum regions are not drawn to scale.

Figure 9. Illustration of the experimental setup for the irradiation of Cr sample submerged in water.



Graphical Table of Contents

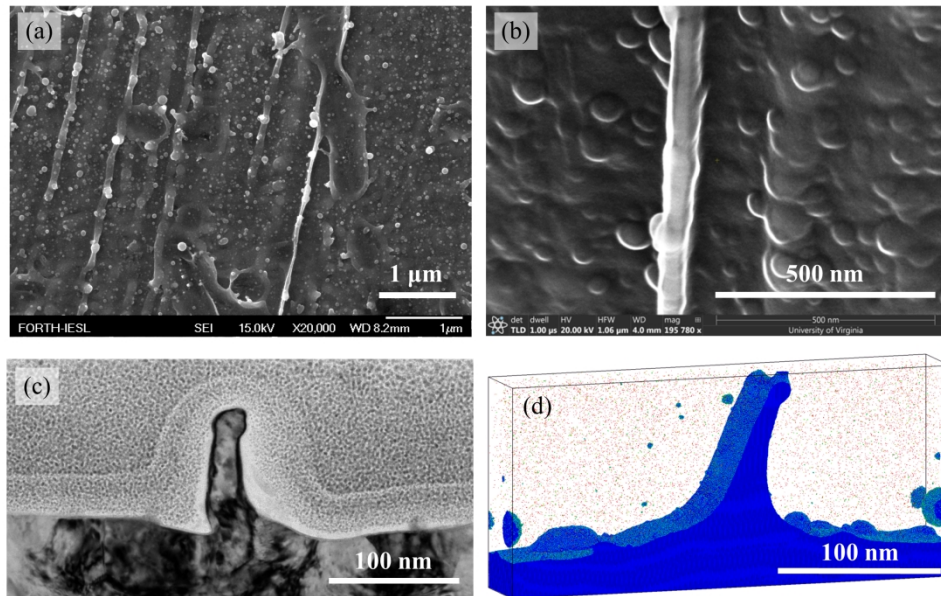


Figure 1. Caption is provided in the text of the paper.

254x190mm (300 x 300 DPI)

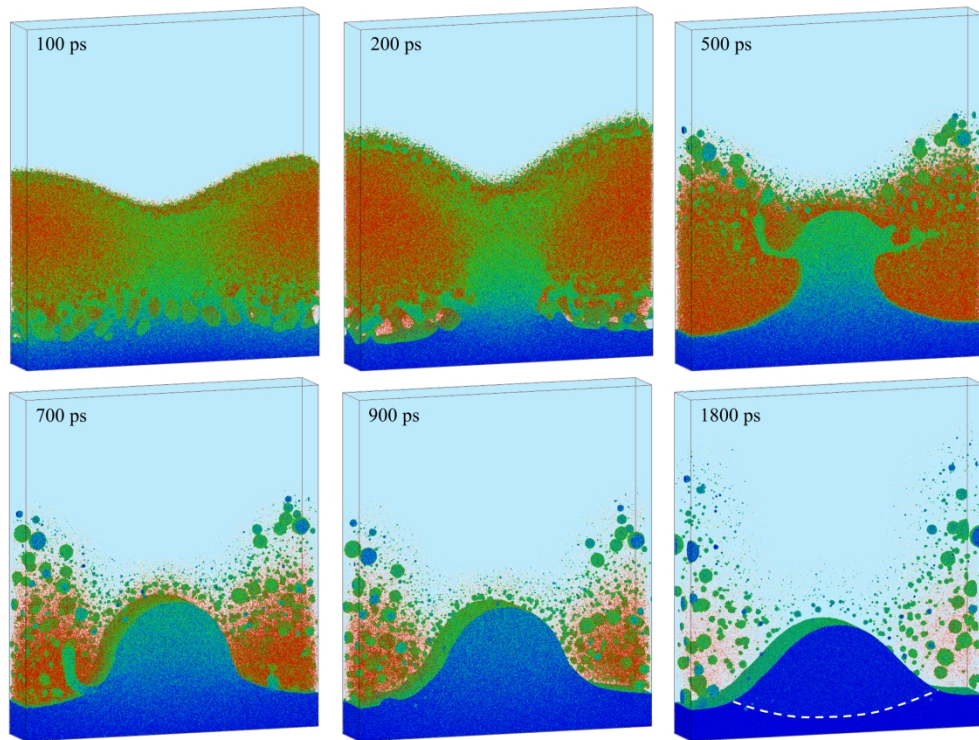


Figure 2. Caption is provided in the text of the paper.

254x190mm (300 x 300 DPI)

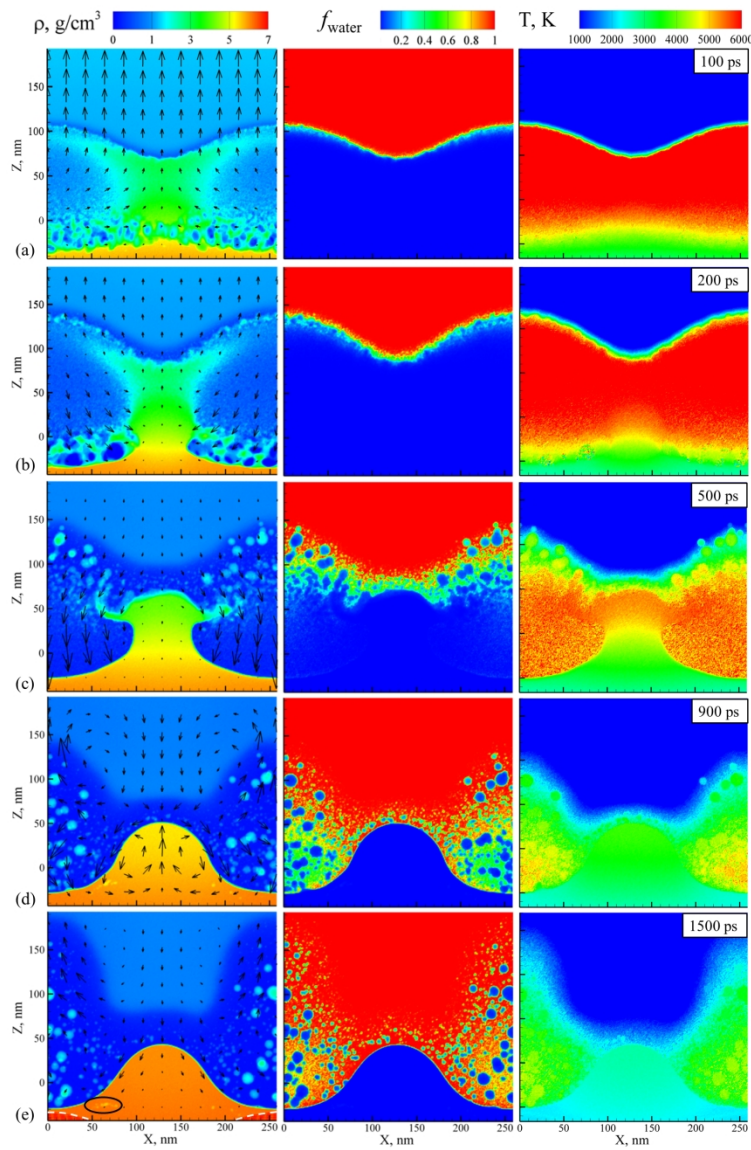


Figure 3. Caption is provided in the text of the paper.

154x243mm (300 x 300 DPI)

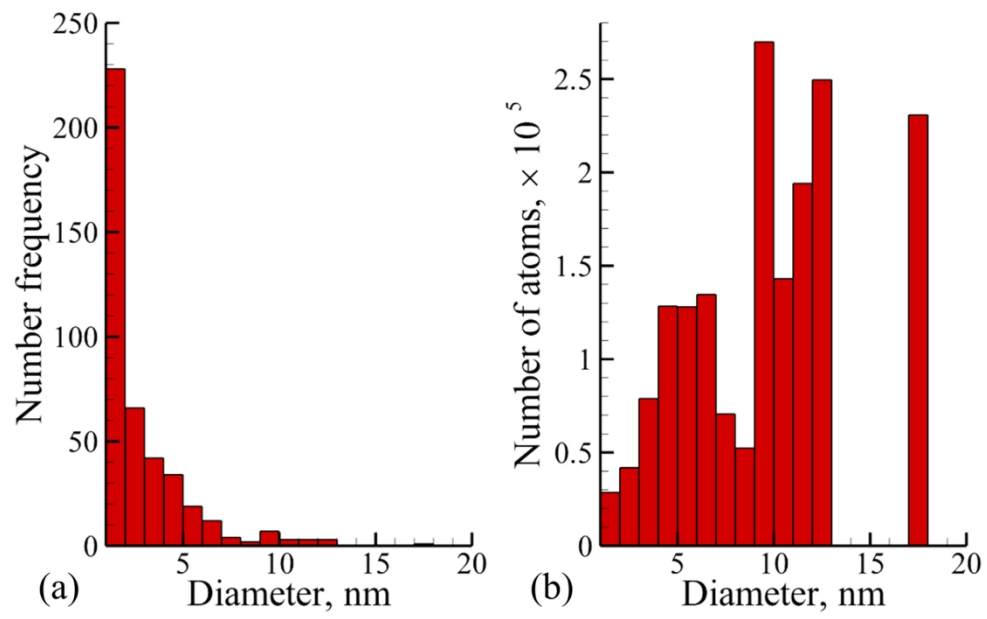


Figure 4. Caption is provided in the text of the paper.

149x97mm (300 x 300 DPI)

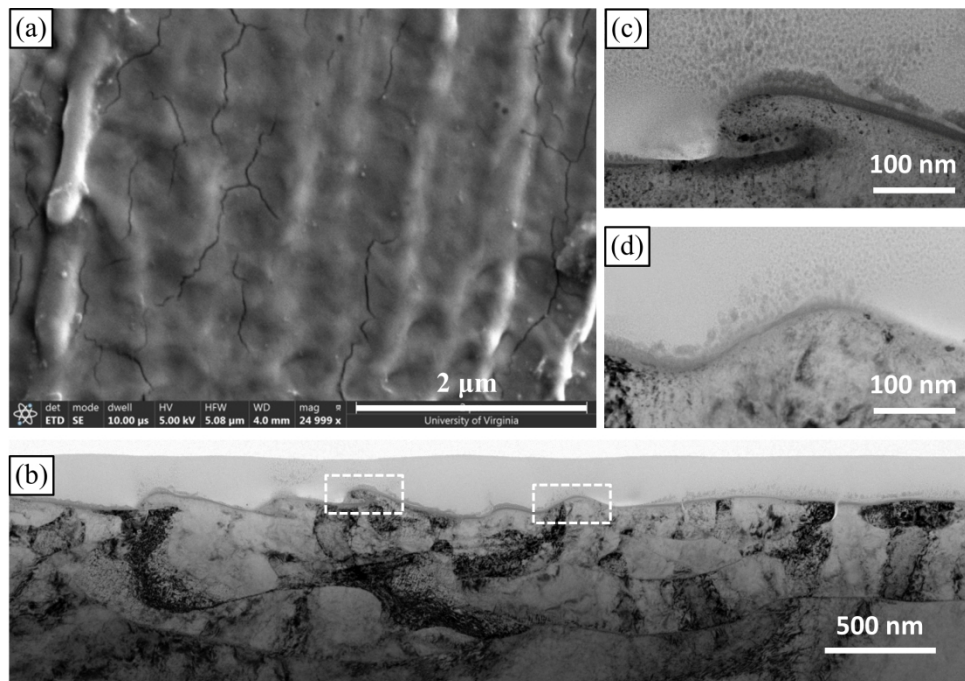


Figure 5. Caption is provided in the text of the paper.

772x546mm (96 x 96 DPI)

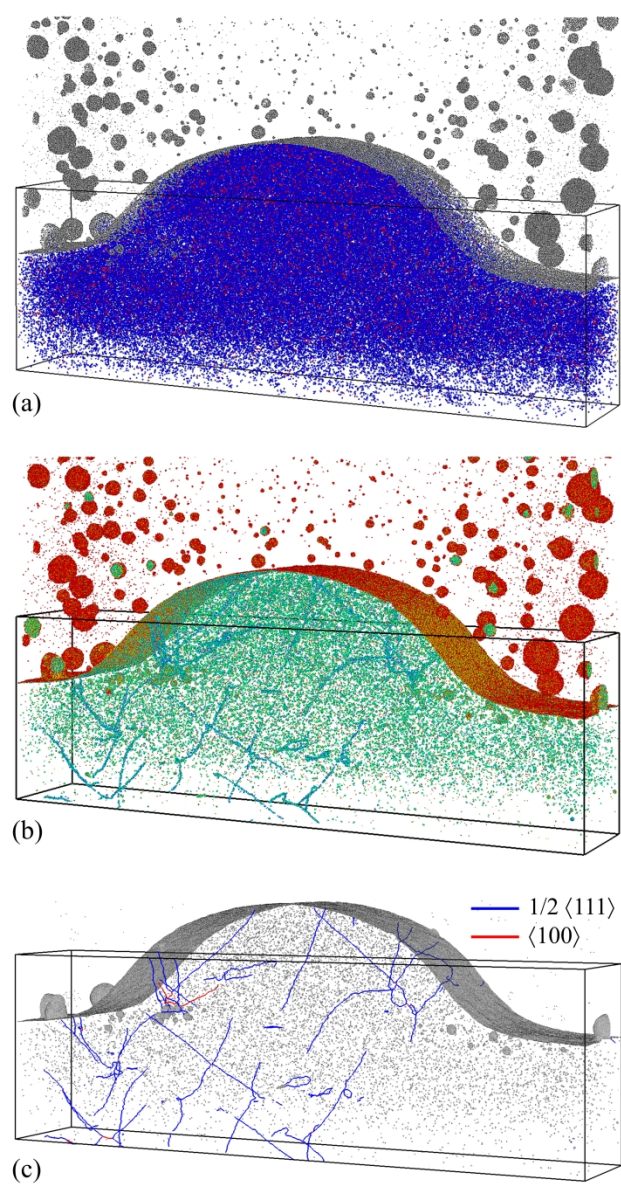


Figure 6. Caption is provided in the text of the paper.

330x635mm (300 x 300 DPI)

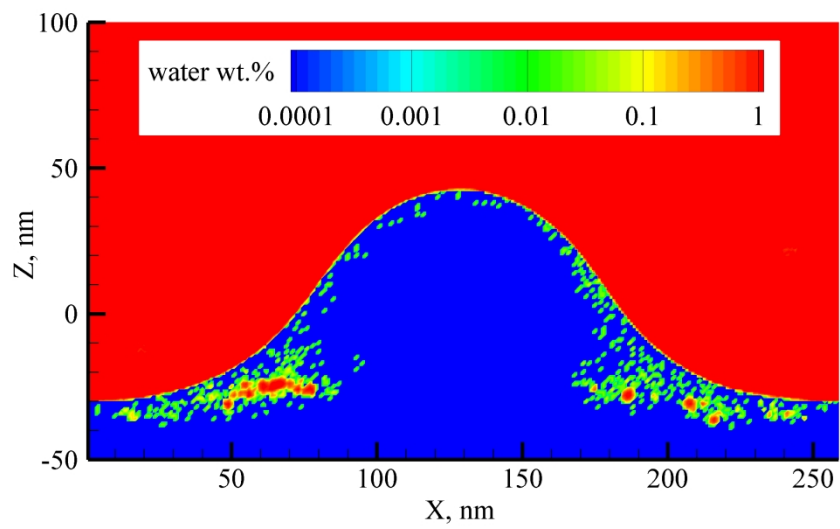


Figure 7. Caption is provided in the text of the paper.

793x705mm (96 x 96 DPI)

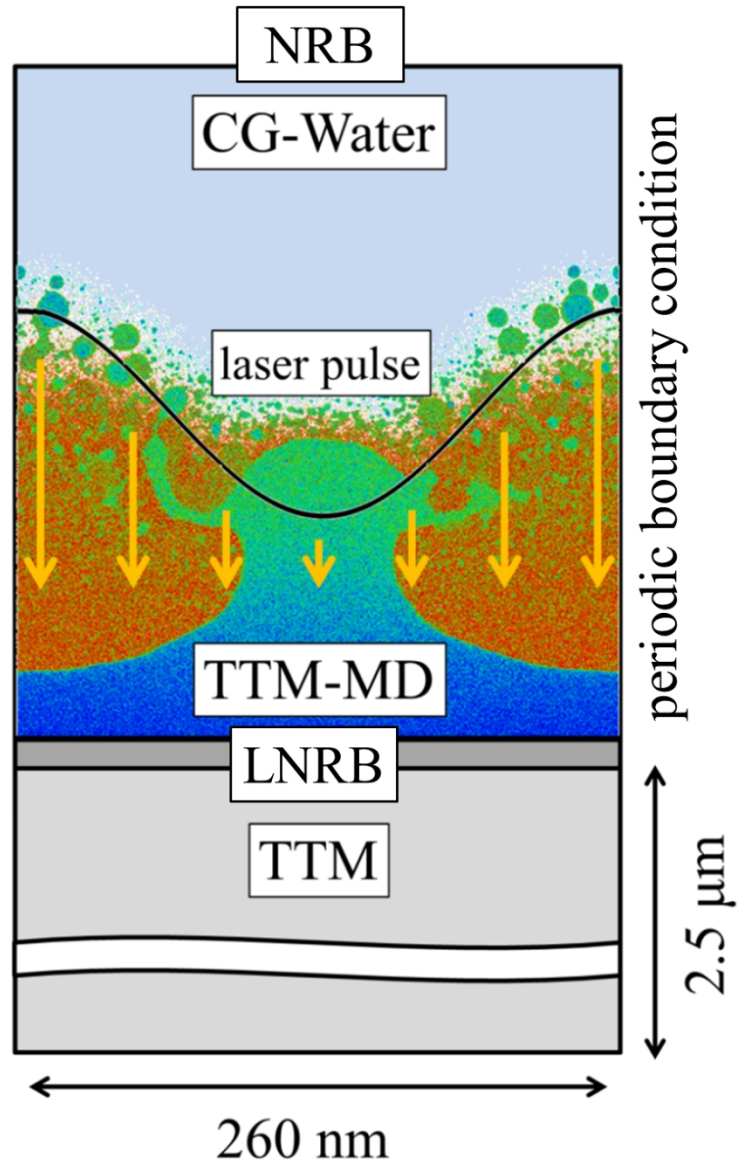


Figure 8. Caption is provided in the text of the paper.

81x127mm (300 x 300 DPI)

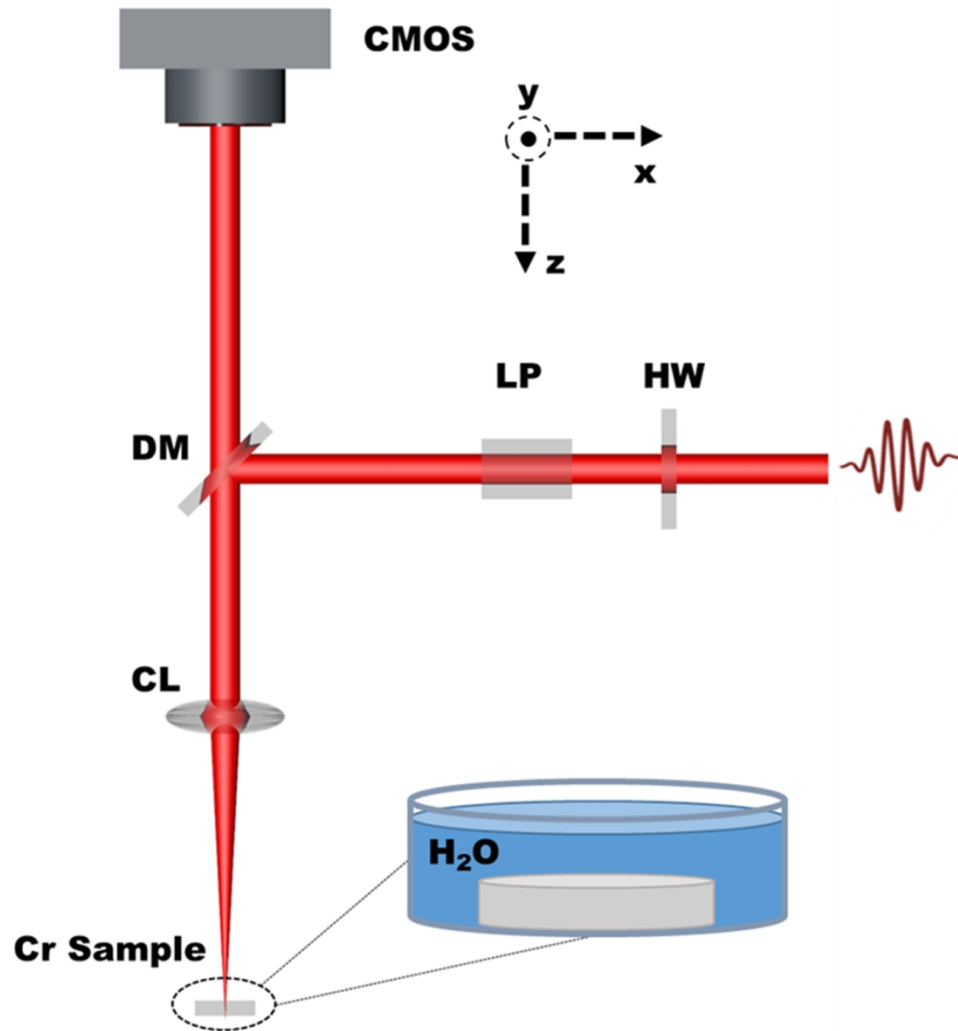
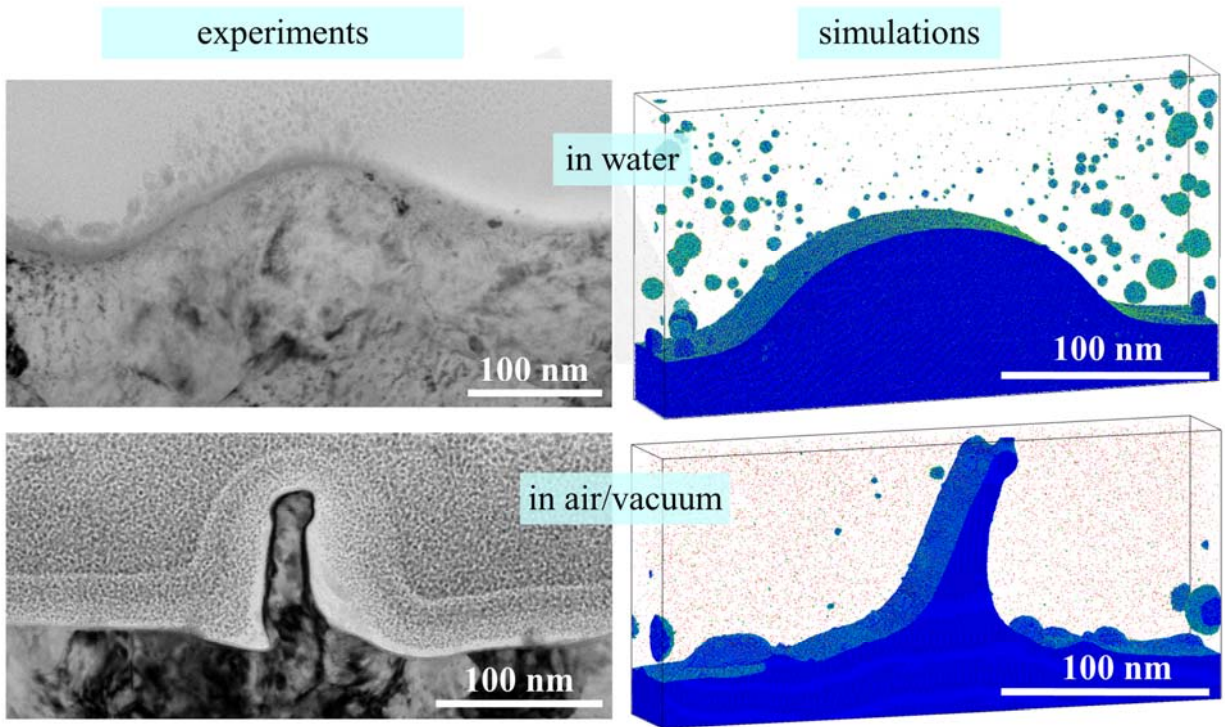


Figure 9. Caption is provided in the text of the paper.

127x132mm (300 x 300 DPI)

Figure for Graphical TOC:

Mechanisms of laser-assisted surface nanostructuring and generation of nanoparticles are revealed in a closely integrated computational and experimental study.